Title

Helical dislocations: Observation of vacancy defect bias of screw dislocations in neutron irradiated Fe–9Cr

Authors

Haley, JC
Liu, F
Tarleton, E
et al.

Publication Date

2019-12-01

DOI

10.1016/j.actamat.2019.09.031

Peer reviewed

Acta Materialia 181 (2019) 173–184

Contents lists available at ScienceDirect

Acta Materialia

journal homepage: www.elsevier.com/locate/actamat

Full length article

Helical dislocations: Observation of vacancy defect bias of screw dislocations in neutron irradiated Fe–9Cr

J.C. Haley[a,*], F. Liu[a], E. Tarleton[a,b], A.C.F. Cocks[b], G.R. Odette[c], S. Lozano-Perez[a], S.G. Roberts[a]

[a] Department of Materials, University of Oxford, Parks Road, Oxford OX1 3PH, UK
[b] Department of Engineering Science, University of Oxford, Parks Road, Oxford OX1 3PJ, UK
[c] UCSB Department of Mechanical Engineering, 2343 Engineering II Building, Santa Barbara, CA 93106-5070, USA

ARTICLE INFO

Article history:
Received 17 May 2019
Revised 4 September 2019
Accepted 19 September 2019
Available online 23 September 2019

Keywords:
Helical dislocation
Dislocation dynamics
Dislocation loop
FeCr
Radiation damage

ABSTRACT

We have analysed the microstructure of a model alloy of Fe9Cr irradiated with neutrons to a dose of 1.6 dpa at 325 °C. Helical dislocations comprise a major part of the damage; these formed from the interaction of pre-existing screw dislocations with irradiation-induced defects. We have investigated the process behind how these helices form, and how they cause local clustering of dislocation loops. Specifically, we have shown experimentally that the interaction of vacancy defects with pre-existing screw dislocations causes the formation of mixed screw-edge helical dislocations. Interstitials and vacancies were generated in equal numbers, which shows that the screw dislocations must have acted as vacancy-biased sinks.

Helical dislocations in general were analysed from a theoretical perspective, and three Dimensional Discrete Dislocation Dynamics (3D-DDD) was used to develop a model for the formation and growth of a vacancy-fed helical dislocation.

Since the helical dislocations cause the removal of vacancies from the local microstructure, this leaves a higher supersaturation of interstitials close to the dislocations. We argue that this supersaturation is responsible for enhanced interstitial loop coarsening, leading to a higher proportion of visible interstitial clusters in the vicinity of helical dislocations. These findings offer a new perspective on how dislocations affect the spatial homogeneity of radiation damage.

1. Introduction

Ferritic-martensitic (FM) steels with chromium content close to 9 at% are prime candidates for use as radiation-tolerant structural materials in both Gen-IV fission and fusion reactors. They are designed to exhibit low activation and display good resistance to swelling and corrosion [1,2]. However, irradiation at temperatures below 500 °C leads to hardening, loss of ductility, and an increase in the brittle to ductile transition temperature [3,4]. These macroscale mechanical changes are caused by the defects that form during irradiation; neutron irradiation inside a fission or fusion reactor can change the microstructure of FM steels through the production of dislocation loops, alpha-prime precipitates, voids and gas bubbles, and segregation of alloying elements, including solute defect cluster complexes [1–7].

The response of FM steels, and their simpler FeCr binary-alloy counterparts, to irradiation is influenced by irradiation dose, temperature, dose-rate, composition, impurity content, grain size and dislocation density [5,6,8–10]. Grain boundaries and network dislocations in particular have been shown to have a strong effect on the homogeneity of the spatial distributions of dislocation loops [11–16], and vast defect-free zones are often observed. Robertson et al. [11] showed vast defect free regions exist in high and low purity iron irradiated with neutrons to a dose of ~0.06 displacements per atom (dpa) at 80 °C. At a higher dose of ~0.2 dpa, the high purity iron contained a uniform distribution of small dislocation loops in regions that had been absent in damage at the lower dose. Matijasevic et al. [17] found no visible defects in single crystal Fe15Cr irradiated to 0.2 dpa at 300 °C, but a uniform dislocation loop spatial distribution in single crystal iron. Hernandez-Mayoral et al. [12], who studied FeCr alloys ranging from 2.5%Cr to 12%Cr irradiated with neutrons to 0.6 dpa at 300 °C, found a uniform distribution of loops in Fe2.5Cr, but vast defect-free regions in all other alloys, with loop clustering at dislocations and

* Corresponding author.
E-mail address: jack.haley@materials.ox.ac.uk (J.C. Haley).

https://doi.org/10.1016/j.actamat.2019.09.031

grain boundaries. Since defect mobility is reduced by impurity and alloying elements, these studies all indicate heterogeneous spatial distribution of dislocation loops is more significant when defects are less mobile (and does not necessarily correlate with the formation of chromium-rich α'-phases [12,16]). While the phenomenon appears to be dose-dependent, the residual dislocations and grain structure were considered by English [13] to be pre-requisites for such heterogeneous distributions.

Schäublin et al. [18] showed that ~1 nm dislocation loops can nucleate at very low doses (~10^{-3} dpa) in Fe14Cr during an in-situ irradiation experiment (room temperature, 500 keV Fe+ ions and 6×10^{-5} dpa/s) to give a defect density of ~1×10^{21}/m^3. This suggests that so-called defect-free zones seen in prior studies [11,12,17] may actually contain small defects, below the resolution of those experiments. Chen et al. [16] also saw dislocation loops in Fe10Cr irradiated to 0.01 dpa with neutrons at 300 °C, but at a larger size (~3.5 nm) than those seen by Schäublin et al. in the Fe14Cr, and at a much lower density of ~2×10^{19}/m^3.

The mechanism behind how radiation-induced dislocation loops come to decorate dislocations is unclear. A suggested explanation by Trinkaus et al. [19,20] is that the one-dimensional movement of interstitial clusters is biased towards dislocations due to their strain field, which leads to an increase in density of observable interstitial loops in these regions. An issue with this argument is that it should be more significant for circumstances where the defects are more mobile, which is against what has been observed experimentally [12].

Irradiation induced point defects and loops may also combine with pre-existing dislocations by inducing climb [14,21,22]. Defect-mediated climb on screw-dominated dislocations can cause the formation of helical dislocations during irradiation, similar to those often seen in quenched materials [23]. Such helical dislocations have been seen in irradiated materials [11,13,21,24,25], but they are rarely acknowledged or discussed in detail in the general irradiation effects literature, including most modelling studies of damage accumulation that include dislocations as point defect sinks.

The formation mechanism of helical dislocations during irradiation is unclear, as is their influence on the surrounding microstructure. Since vacancies and self-interstitials are produced in equal quantities under neutron irradiation, the observation of helical dislocations in irradiated materials implies the screw dislocations must bias one defect type over the other.

As self-interstitials are often the more mobile of the two defect types [26], it might be expected that they would dominate the defect accumulation close to the dislocations. This is suggested as an explanation by Schäublin et al. [21] for helical dislocation formation during irradiation. Higher densities of interstitial clusters close to the dislocation would then be expected, some of which may react with the screw dislocation to produce a helix. The theory behind the prismatic loop/screw dislocation interaction has previously been studied [27–29]; however, these examples consider the interaction in the context of plastic deformation, where the prismatic dislocation loops act as obstacles for screw dislocations gliding through the crystal, instead of dislocations acting as sinks for loops and other defects (as would be the case during irradiation).

Schäublin et al. [21] reason that the movement of interstitial ⟨111⟩ dislocation loops towards the screw dislocations would also increase the rate of dislocation loop coalescence, leading to an increase in ⟨100⟩ loop formation via the 111-mechanism [30]. However, recent calculations by Chang et al. [31] suggest that screw dislocations in iron have an overall bias towards being vacancy sinks, casting doubt over whether interstitial loops are responsible for the formation of helical dislocations during irradiation.

The evolution of BCC alloy pre-existing dislocation structures is critically important to a wide range of radiation effects work, including sink strengths in rate theory (RT) and kinetic lattice Monte Carlo (KLMC) models [32,33]. Here we report on a comprehensive investigation into the formation of helical dislocations in a neutron-irradiated alloy of Fe9Cr, and of the irradiation-induced defects that were found close to the dislocations. Our analysis has led to new insights into the source of these helical dislocations, with implications for the process behind heterogeneous spatial distributions of dislocation loops and the defect bias of screw dislocations in iron-based BCC alloys.

2. Methods

A model alloy of Fe9Cr was studied for this work; the same alloy was also studied by Gelles in the 1980s as part of the fast breeder reactor program [5], and more recently by Bachhav et al. [6] and Bhattacharyya et al. [34]. In atomic-percent, the alloy comprises 9.36% Cr, 0.05% Ni, 0.02% V, and 0.01% each of C, Si, P and Mn (see APT study by Bachhav et al. [6]). Prior to irradiation, the material was cold rolled, then annealed in an argon atmosphere at 950 °C for 15 min and at 750 °C for 1 h, with air-cooling after each anneal. This resulted in a ferritic grain structure with sizes from a few microns up to 100 µm, and a low dislocation density (~6×10^{12} m^{-2}).

The Fe9Cr was irradiated in the Advanced Test Reactor (ATR) at Idaho National Laboratory at a temperature of 315–335 °C (min-max) over 202 days [35,36]. The neutron fluence was 1.2×10^{25} n/m^2 (E>1 MeV) which corresponds to a dose of 1.6 dpa at a rate of 9.4×10^{-8} dpa/s, as calculated using FISPACT-2 with the TENDL-2014 neutron cross-section library [37] and SPECTER-modelled [38] ATR neutron-fluence spectrum [35]. The conditions of this irradiation differ to the study by Bachhav et al. [6] and Bhattacharyya et al. [34] only in dose rate.

The sample was prepared post-irradiation by electropolishing the surface to remove surface deformation, followed by TEM sample preparation via the Focussed Ion Beam (FIB) lift-out method [39] at the Center for Advanced Energy Studies in Idaho USA, and the UKAEA Materials Research Facility in the UK. Jet-electropolishing was not used since the volume of material available was too small. To remove 30 kV Ga+ FIB damage, a final thinning from ~180 nm foil thickness to ~100 nm was conducted using 2 kV Ga+ ions.

The samples were examined at the University of Oxford by a JEOL 2100 L TEM operating at 200 kV with a LaB_6 source. The time between sample preparation and examination was less than a day for the first imaging in order to minimise oxidation, but in spite of this, the formation of a thin oxide layer could not be avoided. Micrographs were captured using dark-field conditions with deviation parameters varying from ~0.07 to ~0.25 nm^{-1}. Precession of the electron beam was used to capture 10 exposures with slightly varying deviation parameter (approximately ±0.017 nm^{-1}) automatically, in a similar manner to the technique demonstrated by Prokhodtseva et al. [40]. Use of electron beam precession via scripted beam control allows the acquisition of several deviation parameters (as recommended by Kirk et al. [41]) without the need to calibrate the crystal orientation. This process is shown in supplementary material 1 (SM-1), and further discussion can be found in [42]. The images were aligned and stacked in FIJI [43] to produce a single micrograph with reduced extinction distance-related absences of defects.

A three-dimensional discrete dislocation dynamic (3D-DDD) method [44,45] was employed to provide insight into the combined glide/climb processes which occur under neutron irradiation. As a time and temperature dependent process, diffusion-controlled climb occurs over a timescale that is too long to be captured by atomistic simulation, and the characteristic length-scale of detailed dislocation configurations is much smaller than is accessible with continuum theory [46]. As an alternative, the 3D-DDD method di-

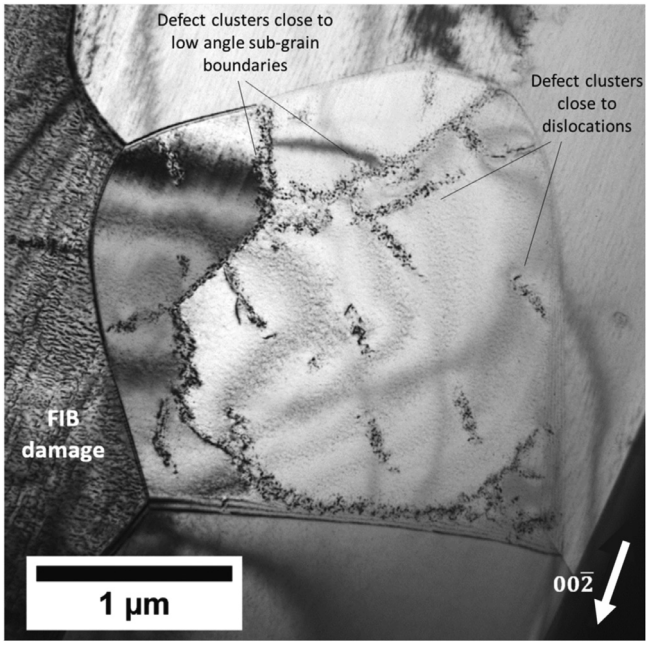

Fig. 1. Low magnification micrograph of a typical grain in the neutron irradiated Fe9Cr, captured in kinematical bright field conditions.

rectly deals with the dislocation lines and bridges the atomistic and continuum domains. It is thus well suited for modelling dislocation interactions with the irradiation-induced defects studied in this work.

The nodal DD method was developed based on the elasticity theory of dislocations [47,48], in which arbitrarily shaped dislocation lines are discretised into straight dislocation line segments with arbitrary orientation bounded by two nodes. At each time increment the force, velocity and position of the nodes is updated and the plastic deformation is described by the motion of the dislocation segments. In the DD framework used here, the dislocation climb rate (assuming a steady-state vacancy bulk diffusion) is determined by the vacancy volumetric flux across the dislocation core [49–51]. The glide mobility follows a linear drag law [45]. The glide and climb mobility are then implemented into the DD framework to obtain the nodal velocities which drive the evolution of the dislocation network. A sequentially coupled time scheme [49] is employed to bridge the huge time scale separation between glide and climb.

3. Experimental results

Fig. 1 shows a kinematical bright field image of a single grain at low magnification. A low angle sub-grain boundary is visible in the central grain (separating the light and dark regions of the grain), around which dislocation loops have segregated. The short bands of contrast visible inside the grain result from pre-existing dislocation lines, around which dislocation loops have clustered. No dislocation loops were found segregated around the high-angle grain boundaries.

Fig. 2 shows two higher magnification micrographs of one of the dislocation lines, around which dislocation loops are visible. The images were captured with the electron beam oriented close to [100] (Fig. 2a) and [1$\bar{1}$0] (Fig. 2b) in order to show the 3D geometry of the dislocation. The micrographs show that the dislocation line is helical, and that within the helix is a high density of visible dislocation loops. The helical dislocation is shown graphically also in the insert in Fig. 2a. The helix has an average diameter of 72.5 ± 5.0 nm, ignoring the ends of the helix where it narrows due to surface effects. The periodicity of the helix is 66.7 ± 6.8 nm on average. Convergent Beam Electron Diffraction (CBED) indicates a foil thickness [52] in this region of 103 ± 10 nm. Fig. 2 also shows that while dislocation loops are found inside the helical dislocation, their density is very low outside the helix. Although some black-dot damage was visible outside the helix, this was mostly indistinguishable from FIB damage or oxide (examples shown in SM-2 and SM-3).

3.1. Dislocation Burgers vector analysis and loop density

Fig. 3 shows additional g-vector conditions used to identify the Burgers vector $\boldsymbol{b}$ of the helical dislocation. To satisfy the $\boldsymbol{g}\cdot\boldsymbol{b}$ invisibility criterion [53], the Burgers vector of the dislocation must be $\pm[11\bar{1}]$. The core of the helical dislocation points close to $\pm[55\bar{4}]$, which is ~6° from the $[11\bar{1}]$ direction, indicating the dislocation was initially mostly screw type.

By the same $\boldsymbol{g}\cdot\boldsymbol{b}$ method [53], we deduce that all dislocation loops inside the helix are ⟨111⟩ type, since no loops were visible in both 011 and $0\bar{1}1$ conditions (assuming all ⟨100⟩ variants are equally probable). Furthermore, none appear edge-on and oriented with ⟨100⟩ directions, as would be expected of such loops viewed close to a ⟨100⟩ zone axis. These dislocation loops were then counted in weak-beam conditions $\boldsymbol{g}=\pm 011$, $\pm 01\bar{1}$, $\pm 11\bar{2}$, $\pm 12\bar{1}$, ± 112 and ± 121 (deviation parameter ~0.2 nm^{-1}), with 80–100 loops counted in each condition (see SM-4). We only considered loops larger than 2 nm for the number density and Burgers vector analysis because counting was very ambiguous for loops smaller

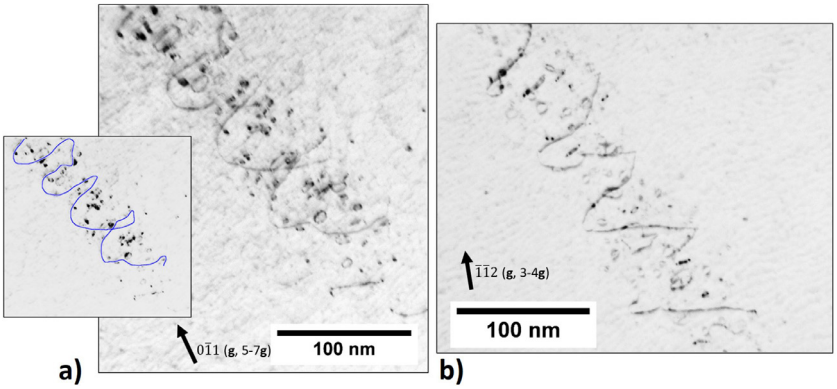

Fig. 2. Higher magnification micrographs a dislocation in the neutron irradiated Fe9Cr, captured in weak-beam dark field conditions (shown with inverted contrast). For (a), the image was captured close to a [100] zone axis. For (b), the image was captured close to a [1$\bar{1}$0] zone axis.

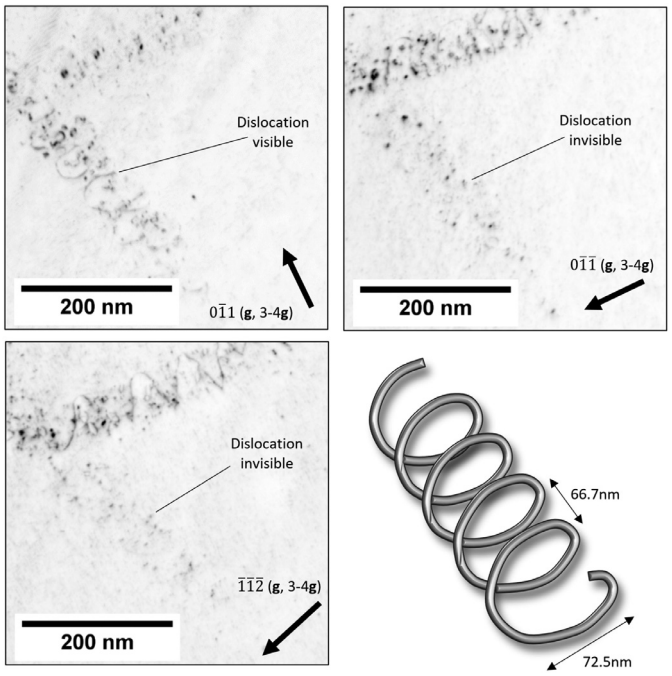

Fig. 3. A series of weak-beam dark field micrographs (shown with inverted contrast), captured using several g-vectors. From the $\boldsymbol{g}\cdot\boldsymbol{b}$ invisibility criterion, the helix has a Burgers vector of [11$\bar{1}$]. The helix is also shown graphically. A different helical dislocation is also visible in the 0$\bar{1}\bar{1}$ and $\bar{1}\bar{1}$2 conditions at the top of the micrographs, which has $\boldsymbol{b}$=[111].

than this, and because such small features are often indistinguishable from FIB damage or surface oxide.

By considering the volume enclosed by the helical dislocation, the number density of dislocation loops was determined by statistical analysis [40] (shown in SM-4) to be $1.2\pm0.3\times10^{23}$ loops/m^3 (for loops >2 nm). This analysis also suggests that dislocation loops with $\boldsymbol{b}$=[11$\bar{1}$] are ~15% more frequent than other ⟨111⟩ variants. Far from the helical dislocations and low-angle sub-grain boundaries, the microstructure was absent of loops distinguishable from background noise for hundreds of nanometres. A region measuring 680 × 320 nm was considered as a typical low-loop-density region, and was found to contain only one loop greater than 2 nm in size, which makes the number density in this region of the order of $2\pm1\times10^{20}$ loops/m^3 (for loops >2 nm).

3.2. Inside–outside contrast analysis of dislocation loops

The inside–outside contrast method [54] was used to determine the nature of the dislocation loops, as shown for example loops in Fig. 4. Dislocation loops were defined by the right-hand/finish-start convention for this analysis [54,55]. Inside–outside contrast analysis was conducted for 11 dislocation loops and all were found to be interstitial-type. From this analysis, and considering previous analyses of dislocation loops in neutron-irradiated iron (for example, [56]), it is reasonable to assume all visible dislocation loops are interstitial-type. The majority of loops were close to pure edge, since the loop normals were aligned close to ⟨111⟩ directions, although there were some examples of loops lying closer to ⟨110⟩ directions.

3.3. The size of dislocation loops within the helical dislocation

To make an accurate measurement of the dislocation loop size, rather than simply the image size, the size was taken as the average major diameter of the loop as seen in plus and minus $\boldsymbol{g}$ conditions. The mean dislocation loop diameter was found to be 5.1 ± 3.6 nm.

The number of atoms inside a dislocation loop (the cluster size) can be calculated as, $N_0 = A(\boldsymbol{b}\cdot\hat{\boldsymbol{n}})/v_a$ [57] where A is the area projected by the loop, $\hat{\boldsymbol{n}}$ is the unit vector normal to the loop habit plane, and v_a is the atomic volume. By assuming the visible defects are circular and prismatic ⟨111⟩ dislocation loops, $\boldsymbol{b}\cdot\hat{\boldsymbol{n}}$ becomes $\sqrt{3}a_0/2$, and for a body-centred cubic (BCC) lattice ($v_a = {a_0}^3/2$), the equation for cluster size becomes a simple function of the measured loop diameter d,

$$N_0(d) = \sqrt{3}\pi\left(\frac{d}{2a_0}\right)^2 \quad (1)$$

where a_0=0.286 nm is the lattice parameter. The cluster sizes were calculated for each loop, and these were then binned as $0\leq Y<0.1$, $0.1\leq Y<0.2$, etc. where $N_0 = 10^Y$ (i.e. logarithmically-spaced bins), and frequencies of occurrence were normalised against their respective bin-width. This approach was also used by Yi et al. [58] and Sand et al. [59] to ensure each bin contains at least a few data points.

This treatment was used to produce Fig. 5, which shows the size distribution of the dislocation loops by cluster size. Overlaid on the distribution is a power-law function fitted to the distribution for clusters >100 atoms; this power law is a good fit to the experimental distribution for clusters in this range. The total number of interstitial atoms contained by dislocation loops larger than 100 atoms was calculated as $7.7\pm1.5\times10^{25}$ interstitials/m^3, or $2.0\pm0.4\times10^4$ interstitials per helical turn. If we assume the power law is valid for cluster sizes <100 atoms, then the difference between power law and experimental data corresponds to an additional $4.3\pm0.8\times10^3$ interstitials per helical turn. This then gives a total of $2.5\pm0.5\times10^4$ interstitials per helical turn ($9.4\pm1.8\times10^{25}$ interstitials/m^3), assuming no vacancy loops were present (as implied from the analysis in Section 3.2).

3.4. Inside–outside contrast analysis of the helical dislocations

The helical dislocations are a product of the radiation damage, since only straight screw dislocations were observed in the unirradiated material. Helical dislocations take shape when a near screw or mixed character segment bows out by dislocation climb due to absorbing or emitting point defects, resulting in a mixed screw/edge helical dislocation. Theoretical analyses of the formation of such helices have been extensively discussed in the literature, for example [23,60,61].

It is possible to verify whether the flux of defects that produced the helical dislocation in the neutron-irradiated Fe9Cr was predominantly interstitial or vacancy by using the same inside–outside contrast analysis used to determine the nature of the loops [62]. The inside–outside technique can measure whether the material within the helix is in compression or tension. If we treat the helix as an array of non-edge dislocation loops, we can determine whether the "loops" are interstitial or vacancy, and hence whether the helix formed from vacancies or interstitials. Fig. 6(a) and (b) shows the inside–outside contrast behaviour for the helix when $\boldsymbol{g}$=01$\bar{1}$ and $\boldsymbol{g}$=0$\bar{1}$1.

Fig. 6(c) depicts the contrast schematically for an analogous prismatic loop, from which it can be concluded that the helical dislocation must have been produced by vacancy-mediated climb. Since the helical shape was produced by vacancy absorption, and it is a left-handed helix, the initial screw dislocation must also have been left-handed [23,63].

This analysis was conducted on two other helical dislocations, including a helix with a steeper inclination in the foil to rule out unsafe orientation effects [54] (shown in SM-5). In all instances,

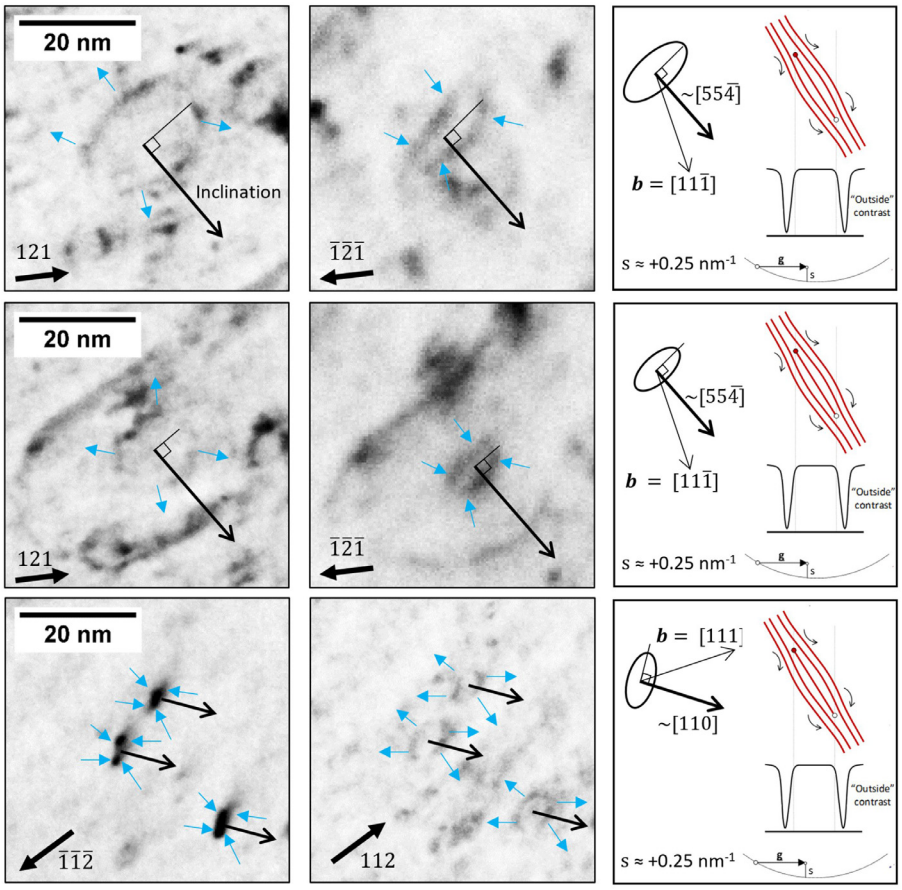

Fig. 4. Nature analysis of a selection of dislocation loops in the neutron irradiated Fe9Cr using weak-beam dark field conditions (shown with inverted contrast). The Burgers vectors were determined by correlating the same feature through a full $\boldsymbol{g}\cdot\boldsymbol{b}$ series and by tilting to observe the inclination. All loops were found to be interstitial.

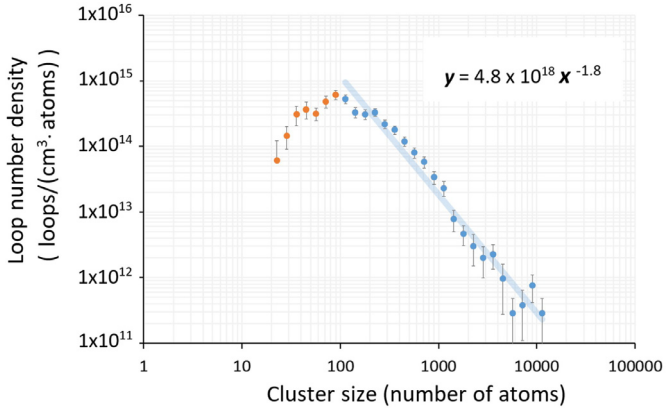

Fig. 5. Dislocation loop size distribution by atomic volume. The blue points indicate those used to fit a power-law. The points represent bins that are logarithmically spaced, and the frequency of counts within each bin has been normalised to loop number density (loops/m^3) and the bin-width (atoms). Error bars are calculated as $\sqrt{N}$, where N is the number of loops counted. (For interpretation of the references to colour in this figure legend, the reader is referred to the web version of this article.)

the helical dislocations were found to be of vacancy type. Therefore, in the presence of equal numbers of vacancies and self-interstitials produced continually by irradiation, the screw dislocations must be acting as vacancy-biased sinks.

Each turn of a helix will have absorbed the same number of defects as those contained by a prismatic dislocation loop of equivalent diameter [23]. From this, it can be calculated from

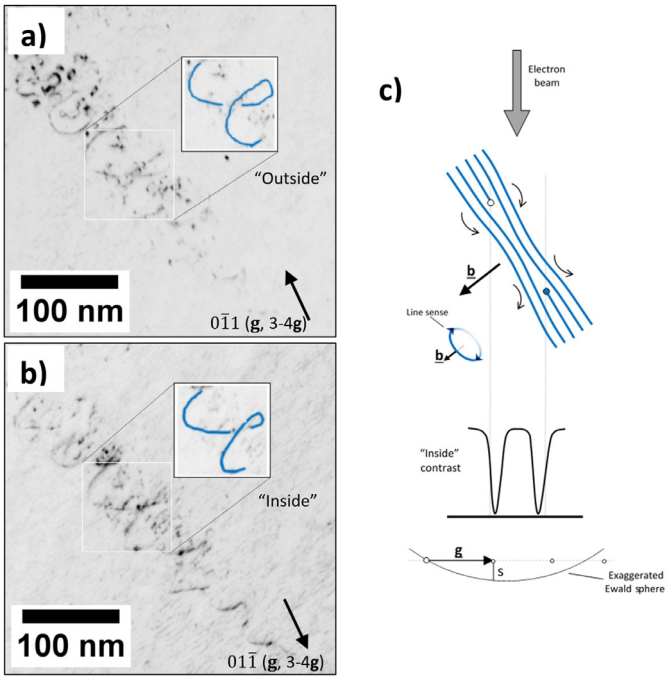

Fig. 6. (a) and (b) show the inside–outside contrast of the helical dislocation. (c) is a diagram depicting the "inside" condition for a vacancy dislocation loop. This analysis shows the turns of the helical dislocation are akin to vacancy dislocation loops, so the climb-mechanism that produced the helical dislocation must have been caused by vacancies.

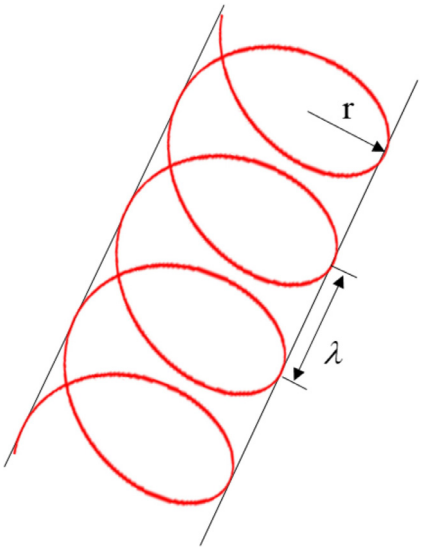

Fig. 7. Schematic of a uniform helix

(1) that $8.8 \pm 1.2 \times 10^4$ vacancies per helical turn ($3.3 \pm 0.5 \times 10^{26}$ vacancies/m^3) were required to cause the climb observed. Since this sample was neutron irradiated, the number of interstitials and vacancies produced by irradiation should be equal, yet we have already estimated from the interstitial loops a population of $2.5 \pm 0.5 \times 10^4$ interstitials per helical turn. The difference implies there must be $6.7 \pm 1.3 \times 10^4$ interstitials per helical turn ($2.6 \pm 0.5 \times 10^{26}$ interstitials/m^3, and $3.0 \pm 0.6 \times 10^{-3}$ interstitials/atom) "missing" from the volume within the helical dislocation; they could be either genuinely no longer present, or present as defects below experimental resolution, or a combination thereof.

4. Analysis of helical dislocation formation

4.1. Theoretical overview and analysis of the formation of helices

A general solution for the energy of a helix with a uniform pitch λ and a radius r, as shown in Fig. 7 was proposed by De Wit [61] based on asymptotic limits of loose winding ($\lambda >> r$) and tight winding ($\lambda << r$).

The equilibrium configuration of a helical dislocation is reached when the energy change due to the growth, ΔW, is balanced by the chemical potential caused by the supersaturation of the point defects. According to the theoretical analysis in Hirth and coworkers [63], the total energy change for a general helix of length, L, can be expressed as,

$$\Delta E = \frac{\Delta W}{L} - \bar{G}\frac{N}{L} \tag{2}$$

The first term, $\Delta W/L$, denotes the increase in energy per unit length of helix, which is contributed from the line tension Γ_{line} and the elastic repulsive force F_e between helical turns. De Wit [61] derived the general solution for the energy of a uniform helix and demonstrated that the solution is intractable except in the limits of tight-winding and loose-winding. For a general helix, as demonstrated in Fig. 3, with a pitch λ=66.7 nm and a radius r=36.3 nm, no explicit expression for ΔW is available and numerical calculation is needed.

The second term in Eq. (2), $\bar{G}$, is the chemical potential per point defect. It creates a thermodynamic driving force – the chemical force F_c [64] – which acts to remove the supersaturated defects from the solution and promotes dislocation climb-related processes. $\bar{G}$ is given as [60],

$$\bar{G} = kT\ ln\left(\frac{c}{c_0}\right) \tag{3}$$

where c is the concentration of the point defects, c_0 is the reference-state concentration of point defects, $c_0 = exp(-\frac{E_f}{kT})$, with E_f denoting the formation energy of the point defect. Eq. (3) does not specify a vacancy or interstitial supersaturation. Therefore, in the absence of a dislocation-bias, the vacancy and interstitial supersaturations should both contribute to the dislocation climb, and a helix will not develop. Since helical dislocations did form during irradiation in our experiment, and the results in Section 3.4 confirm these helices are vacancy-type, the following discussion about helical dislocations only considers vacancies as the source for screw-dislocation climb. The interaction between interstitial loops and helical dislocations is considered at the end of Section 4.2.

The equilibrium condition of the helix is achieved when,

$$\frac{\partial \Delta E}{\partial r} = 0 \tag{4}$$

By substituting Eqs. (2) and (3) into Eq. (4), one may find that it is the balance between the chemical force and the configurational force (including the line tension and elastic repulsion) that determine the shape of the helix.

To derive the vacancy supersaturation c^v/c_0^v associated with the geometric parameters which define the shape of the equilibrium helix, λ and r, a discrete dislocation analysis [49] is employed. In this calculation, the total elastic energy of the helix is calculated using a double linear integral [45]. The driving forces are defined as the negative derivative of the total energy with respect to the dislocation positions.

A large enough chemical force F_c applied to a perfectly straight near-screw dislocation line will cause it to grow into a helix. As the helix grows, the ordinary force (composed of line tension and the elastic interaction) also increases. We define a configurational force F_{con} to express the ordinary force per length caused by the configuration of dislocation line. An equilibrium helical configuration is obtained when the chemical force F_c is balanced by the configurational force F_{con}. The chemical force F_c is approximately [52],

$$F_c = \frac{kTb}{\nu_a}\ ln\left(\frac{c^v}{c_0^v}\right) \tag{5}$$

The direction of the chemical force F_c is,

$$\hat{\boldsymbol{n}} = \frac{\hat{\boldsymbol{l}} \times \boldsymbol{b}}{\left|\hat{\boldsymbol{l}} \times \boldsymbol{b}\right|} \tag{6}$$

with $\hat{\boldsymbol{l}}$ denoting the unit line direction and $\boldsymbol{b}$ representing the Burgers vector. Therefore, it is the final equilibrium configuration that matters in calculating the corresponding vacancy concentration, which is calculable via static DD analysis. For details about how to calculate these forces in DD, please refer to [39].

A plot of configurational force/per length versus different helical radius, r, for the case where the wavelength λ =66.7 nm, is shown by the blue curve in Fig. 8. The red line indicates the chemical force necessary to balance the configurational force when r =37.0 nm or 83.0 nm. Only the curve for r =37.0 nm gives stable equilibrium because of the lower energy state. Therefore, the vacancy supersaturation, c^v/c_0^v, needed to maintain a helix with λ=66.7 nm and r = 36.3 nm at T=600 K (such as that shown in Fig. 3), is ~900.

4.2. 3D-DDD modelling of the formation of helical dislocations

To illustrate the detailed creation process of the helix, a 3D-DDD simulation for a vacancy supersaturation c^v/c_0^v=900 was also conducted.

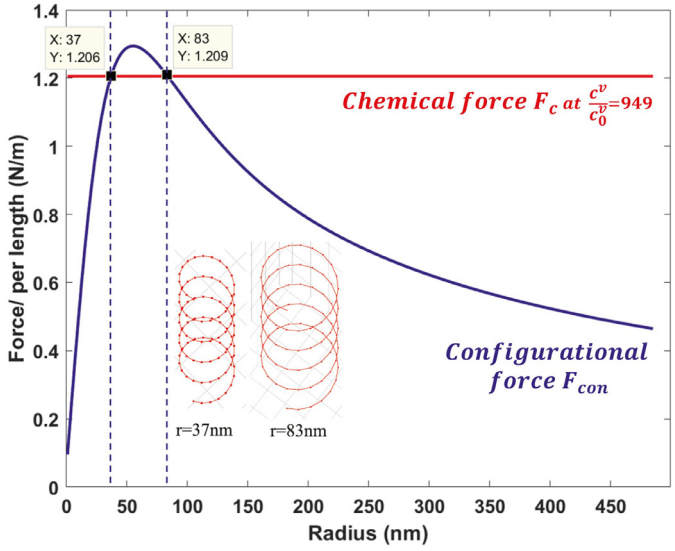

Fig. 8. Static DD analysis of configurational force versus helical radius r for the case λ =66.7 nm. (For interpretation of the references to colour in this figure legend, the reader is referred to the web version of this article.)

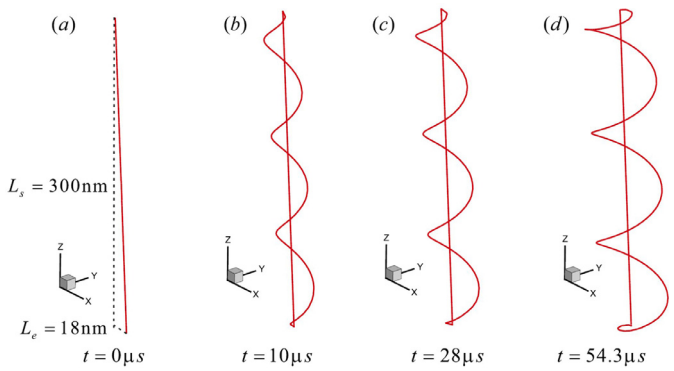

Fig. 9. Dislocation configurations during the evolution.

Table 1
Parameters for α-iron.

Parameters	Magnitude
Shear Modulus	μ=83 GPa
Poisson's ratio	ν=0.29
Lattice parameter	a_0=2.856 Å
Burgers vector	$b=\sqrt{3}\ a_0/2$
Drag coefficient of edge component	$B_e=5\times10^{-4}$ Pa s
Drag coefficient of screw component	$B_s=1\times10^{-2}$ Pa s

The 3D-DDD method used here has been described in detail in [49], and to accelerate the 3D-DDD simulation, a Graphical Processing Unit (GPU) was used [65,66]. Both dislocation glide and climb were considered in the model, using a dislocation glide mobility law for a BCC crystal [45]. In BCC crystals, there is a significant difference between the mobility of screw and edge dislocations. The drag coefficient of a pure edge dislocation, B_e, is smaller than that of the pure screw, B_s. In addition, screw dislocations are assumed to have an isotropic mobility in all directions perpendicular to the line, while the drag coefficient for non-screw dislocations is anisotropic (glide being usually rapid, while climb is generally slow and controlled by diffusion). The drag coefficient of a mixed dislocation segment was calculated based on an interpolation function [44],

$$\boldsymbol{B}(\boldsymbol{\xi}) = b\left[B_e^{-2}\left\|\boldsymbol{b}\times\boldsymbol{\xi}\right\|^2 + B_s^{-2}\left(\boldsymbol{b}\cdot\boldsymbol{\xi}\right)^2\right]^{-1/2}(\boldsymbol{m}\otimes\boldsymbol{m}) \tag{7}$$

where $\boldsymbol{\xi}$ is the unit vector of the line direction, $\boldsymbol{b}$ is the Burgers vector with magnitude b, $\boldsymbol{m}$ is the slip direction, B_e is the drag coefficient of pure edge dislocations and B_s is for pure screw dislocations. The glide velocity $\boldsymbol{v}_g$ can then be expressed as,

$$\boldsymbol{v}_g = \boldsymbol{B}(\boldsymbol{\xi})^{-1}\cdot\boldsymbol{f}_g \tag{8}$$

where $\boldsymbol{f}_g$ is the glide component of the mechanical driving force on a node. The Peach–Koehler force, $\boldsymbol{f}_{pk} = (\boldsymbol{\sigma}\cdot\boldsymbol{b})\times\boldsymbol{\xi}$, was integrated along the segments connected to the node, where $\boldsymbol{\sigma}$ is the local stress caused by externally applied tractions and the elastic interactions between every segment pair.

A phonon-drag mobility law was used for dislocation glide, while a lattice diffusion controlled dislocation climb mobility law [64] was used to simulate the climb process, where the climb velocity $\boldsymbol{v}_c$ was derived based on a steady-state diffusion assumption,

$$\boldsymbol{v}_c = \frac{2\pi D_v^0 c_0}{b\sin\theta\ ln(r_\infty/r_c)}\left(\frac{c_{eq}}{c_0}-\frac{c_\infty}{c_0}\right)\frac{\boldsymbol{b}\times\boldsymbol{\xi}}{|\boldsymbol{b}\times\boldsymbol{\xi}|} \tag{9}$$

where D_v^0 is the lattice diffusion coefficient, and θ is the angle between $\boldsymbol{b}$ and $\boldsymbol{\xi}$ which defines the character of the dislocation. The term $\sin\theta$ in Eq. (9) was used because only the edge component of a dislocation segment climbs, and the screw part follows by a quick glissile rearrangement of the atoms [67]. The climb rate was set to zero once the character angle of any segment falls less than 0.01° in order to avoid a singularity occurring. The r_∞ term is the average distance between dislocation segments, r_c is the radius of the cross-section of the area of the dislocation core, and c_{eq} is the equilibrium vacancy concentration,

$$c_{eq} = c_0\ exp\left(\frac{f_c v_a}{KTb}\right) \tag{10}$$

where f_c denotes the climb component of the mechanical driving force $\boldsymbol{f}$, and c_∞ is the average vacancy concentration in the surrounding area.

The time scale separation between (rapid) glide and (slow) climb was bridged in the simulation by a sequentially coupled time scheme [49], in which the increments of dislocation climb per time step were accumulated until at least one slip plane interval was reached [49], defined here as the distance between adjacent (111) planes. The elastic fields were calculated for an infinite domain.

The topology of the dislocation configuration was updated at every increment to deal with the dislocation evolution and determine the type of motion occurring (glide or climb). A straight mixed dislocation with a significant screw component, pinned at two ends, was introduced as the initial configuration, as shown in Fig. 9(a). The Burgers vector was set as [111], parallel to the longitudinal axis. The length of the screw component L_s was 300 nm, and the edge component L_e was 18 nm. The temperature was set to be 600 K. The input vacancy supersaturation was set as c^v/c_0^v=900, as derived from the theoretical analysis in Section 4.1. Other parameters used in the simulation are given in Table 1.

Snapshots of the profiles of the helix at different times during its evolution are illustrated in Fig. 9(b)–(d). A complete video of the formation of the helix is shown in SM-6. The simulation shows the supersaturated vacancy concentration driving the climb of the edge component, which gives rise to a decrease in the wavelength of the helical turns. The growth of helical turns increases the line tension and the interaction between dislocations. The final equilibrium configuration is reached when the osmotic force balances the line tension and the elastic interaction between dislocations. Meanwhile, the elastic interactions between different helical turns also promotes prismatic glide to produce a uniform pitch of the

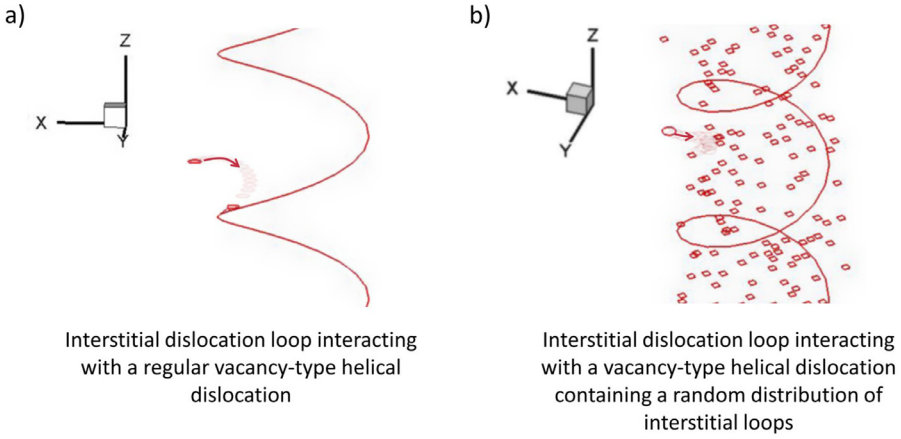

Fig. 10. (a) and (b) are schematic illustrations of a dislocation loop interacting with a helical dislocation based on videos shown in SM-7 and SM-8, respectively. In (a) (SM-7), an interstitial dislocation loop is shown moving towards a vacancy-type helix, and then coalescing with the dislocation line. In (b) (SM-8), the interstitial loop is shown moving towards a vacancy-type dislocation that already contains a random distribution of interstitial loops, in which it will find an equilibrium state within the helix (either positioned within the helix, or coalesced with another dislocation loop).

helix along the dislocation length. Fig. 9(d) shows the equilibrium final configuration with four helical turns. The average wavelength λ was 75.0 nm; the average radius of the loops was also derived from the projection on the (111) plane as r=39.6 nm. This final configuration agrees well with the experimental results (λ =66.7 nm and r=36.3 nm), and the theoretical solutions based on the analysis of de Wit [61] and Hirth and coworkers [63] presented in Section 4.1.

Having modelled the vacancy/screw-dislocation interactions, we will now model the interaction between interstitial loops and helical dislocation, to explain why loops are located inside of the helical turns. The helix modelled in Fig. 9 contains a volume that is vacancy-rich, and hence there is a strong tensile stress field above the slip plane of the dislocation (inside the helix). Interstitial loops would be attracted and approach the helix by a self-climb plus glide mechanism [68], and then interact to form small jogs on it. This interaction is shown in SM-7, and schematically in Fig. 10(a). In SM-8, a different result is obtained when a set of interstitial dislocation loops are already distributed randomly within the volume enclosed by the helix. In this case, the helical dislocation still attracts the approaching interstitial loop, but the loop finds either an equilibrium state inside the helix, positioned among the other interstitial loops; or it will coalesce with another interstitial loop within the helix. The interstitial loops contained by the helix at the start are modelled statically here in order to increase the computational efficiency. The approaching interstitial loop therefore moves rapidly within the helix between a set of static loops as it tries to find an equilibrium state. This is depicted schematically in Fig. 10(b).

5. Discussion

The discussion is divided into two sets of arguments. The first considers the formation of the helical dislocations and the origin of the high density of interstitial loops close to such dislocations. The second considers why the dislocation loop population is so low in regions far from dislocations or grain boundaries.

5.1. Helical dislocation formation in FeCr and local effects

The analyses above explores the origin of helical dislocations in FeCr alloys during neutron irradiation. Experimental data show that the dislocation loops decorating the helical dislocation were of interstitial type, while the helix itself formed from dislocation core interactions with the vacancy population. It is not surprising that interstitials should agglomerate as dislocation loops. The formation energy of an isolated interstitial is larger than that of a vacancy [26]. This leads to a larger osmotic force to remove interstitials from solution, which will agglomerate into stable clusters (interstitial loops) [69]. What is surprising is that these interstitials do not also interact with the screw dislocations to form helices. This implies the screw dislocations act as vacancy-biased sinks.

Edge dislocations generate a tensile/compressive stress field above/below the slip plane, depending on the sign of the dislocation. It is thus easy to understand that interstitials are attracted to the tensile region, and vacancies to the compressive region. This usually leads to the observation of interstitial dislocation loops on one side of an edge dislocation's slip plane [13], since vacancies tend to remain as clusters below the visibility limit (at this temperature and <2 dpa [16]) . A screw dislocation does not generate a hydrostatic stress field, but once it gains edge component as a (proto-) helix, then a bias of one defect type should follow. It might seem that which bias – interstitial or vacancy – is active on a particular screw dislocation would be a matter of chance, with both biases equally probable, leading to the formation of equal numbers of helices formed by the two processes. However, our results imply a defect bias exists prior to the screw dislocation gaining any edge-character.

Chang et al. [31] reasoned that the strong compressive fields very close to a screw dislocation core repel interstitials, whilst vacancies are unaffected. This would allow for a vacancy-driven helix formation process. Chang et al.'s argument follows from their calculations of the bias factors for point defects onto a screw dislocation, where they found that screw dislocations absorb vacancies more efficiently than interstitials. Our experimental measurement of the vacancy-nature of the helical dislocations is thus evidence in favour of Chang et al.'s bias calculations that vacancies are more easily absorbed by screw dislocations.

Interstitials clusters form mostly in-cascade (a fast process), whereas the less mobile vacancies cluster more slowly. Freely migrating interstitials are highly mobile, and so can migrate to sinks away from the cascade region (dislocations, boundaries, or interstitial clusters) or recombine with a vacancy. If interstitial loops are prevented from coalescing with the screw dislocation core, then their presence will exaggerate the vacancy bias by acting as strong sinks for interstitials. This would reduce the amount of recombination occurring after subsequent cascades near screw dislocations,

and leave more vacancies available to drive climb on the screw dislocation. Vacancies are most stable as voids, with vacancy loop nucleation a rare event [70]; we expect the vacancies to interact with the dislocation core as point defects, before they reach post-cascade equilibrium as clusters or recombine with an interstitial. Gilbert et al. [70] estimate the length scale a vacancy migrates before reaching equilibrium as the width of a cascade, typically on the order of 5 nm. This would suggest that the initial vacancy jogs on screw dislocations form from cascades overlapping with the dislocation core.

Though we have included a DD model of helical dislocation growth in this work, further modelling is required to fully understand the interaction between cascades and screw dislocations in iron and other BCC metals. In previous molecular dynamics studies [71,72], it has been shown that cascades overlapping dislocations can stimulate the formation of large vacancy clusters in FCC aluminium [71] (screw dislocation interaction) and HCP zirconium [72] (edge dislocation interaction). In the study of overlap with screw dislocations, interstitial helical segments were also seen.

As the vacancy helix grows, the continued removal of vacancies from the local microstructure will enhance coarsening of the interstitial clusters close to these helical dislocations. Such a mechanism explains the higher density of visible interstitial loops within the confines of the helical dislocations compared to regions far from dislocations and grain boundaries. We have shown that there are more vacancies removed by the helix than there are interstitials contained within visible dislocation loops. This confirms that there is more than enough interstitials available to justify this as an explanation. Interstitials and vacancies were produced in equal numbers, yet the vacancies absorbed by the dislocation outnumber the interstitials contained by visible loops by a factor of 4.3. This implies that there is a large population of interstitials that either escape the helix (which may be easier when the helix is small), or are not visible from the TEM analysis. It may be a combination of the two, where a large fraction of the interstitials exist as either small dislocation loops, or alternative cluster structures such as C15 laves phases [73].

The interstitial nature of the dislocation loops is in agreement with previous analyses of dislocation loops in ferritic materials [11,17,56,74,75], though we note that no ⟨100⟩-type dislocation loops were found in our experiments. The dominant Burgers vector of dislocation loops in ferritic materials undergoes a transition from ⟨111⟩-type to ⟨100⟩-type between 300 and 400 °C [8,76]. The material studied here was irradiated between 315 and 335 °C, and so some ⟨100⟩ loops might be expected; Bhattacharyya et al. [34] studied the same alloy irradiated during the same irradiation experiment (only differing in dose-rate) and also reported mostly ⟨111⟩-type loops. The ⟨100⟩ dislocation loop has been seen experimentally to form from single ⟨111⟩-loops via the rotation of its habit plane [77] and, by Molecular Dynamics modelling, from coalescing ⟨111⟩-loops [78] of different Burgers vectors; which of these mechanisms is more dominant remains unanswered. A lack of ⟨100⟩-loops may indicate a low frequency of loop-loop coalescence, and thus low loop mobility.

Determination of the Burgers vectors by statistical analysis (Section 3.1) suggests a slightly larger fraction of dislocation loops share a Burgers vector with the helical dislocation than other ⟨111⟩ variants (see SM-4). Many of those that have the same Burgers vector as the helix are angled ∼6° from the prismatic plane, and are mostly normal to the core of the helix. Some other ⟨111⟩ variants lie closer to {110} planes than {111}. This suggests there could be a tendency for loops to align themselves with the stress field of the helical dislocation, which may also explain the lack of ⟨100⟩-type loops; the rotation mechanism [77] will be suppressed by there being a preferential alignment, and the coalescence mechanism [78] since loops are more likely to have the same Burgers vector.

The next section will discuss possible reasons why the visible defect population far from the helical dislocations and grain boundaries is so low.

5.2. On the absence of visible damage far from defect sinks

The regions between dislocations and far from sub-grain boundaries contain almost no visible dislocation loops, despite the displacement damage that has occurred. Although a few defects <2 nm in size are visible, this damage is indistinguishable from the 2 kV Ga+ FIB damage visible in unirradiated foils, and in unirradiated electropolished foils containing surface debris and oxide. For comparison, our estimate of the defect density in these regions ($\sim 2 \times 10^{20}$ loops/m^3) is similar to the density of defects seen by Chen et al. [16] in Fe10Cr irradiated with neutrons at 300 °C to only 0.1 dpa.

Three possibilities are considered to explain the lack of visible damage:

(1) The interstitials and vacancies that survive cascades in these regions have recombined.
(2) Point defects or defect clusters have migrated from these regions and were removed by defect sinks (grain boundaries or dislocations), or have clustered around them.
(3) Many of the interstitials and vacancies that survive after cascades in these regions still exist, but in clusters too small to be resolved.

These will each be discussed, but it should be noted that KLMC and RT calculations are ideally required to fully evaluate which is most likely, or whether they all play a role.

The first possibility that the defects have simply all recombined is not unrealistic given the slow dose rate of the neutron irradiation. For a displacement rate of 9.4×10^{-8} dpa/s, a volume of $5 \times 5 \times 5$ nm would see an atom displaced every ∼2 min. Considering that atoms are displaced in large cascades, not as uniformly distributed Frenkel pairs, the time for a cascade to overlap with a previous cascade in the same region is much longer than 2 min (cascade overlap is typical for ∼0.01 dpa, which would take ∼1 day). This is a very long time for primary defects to evolve. If the defects do not migrate far from the cascade core (as may be the case for impure and/or alloyed materials [79,80]), then the surviving defect fraction may be very low when a cascade eventually overlaps. This will inhibit the accumulation of visible damage, and so it may take much higher doses for visible damage to emerge in these regions. This explanation is also argued by Matijasevic et al. [17] and Terentyev et al. [81].

The second possibility seems reasonable on the basis that the visible damage present in the neutron irradiated Fe9Cr is concentrated around sinks – dislocations and sub-grain boundaries. As discussed with respect to the first possibility, the long time for cascade overlap to occur allows for the primary damage to evolve over a relatively long time scale. If interstitial clusters formed in cascades are mobile enough to migrate far away from the core, then they may be able to reach extended sinks such as grain boundaries or dislocations. It is unlikely that the interstitials have migrated far to reach the helical dislocations, as already discussed in Section 5.1, but the origin of the dislocation loops clustered at the low angle sub-grain boundaries has not yet been considered. This population of loops presumably originates from some defect migration towards the boundary. The high angle grain boundaries have no segregation of visible damage, nor any depletion zone. This may indicate that the high angle grain boundaries are very effective at clearing out damage from the bulk. The Fe9Cr material studied here is not ultra-high purity, and contains both substitutional and interstitial impurities. Since defects are easily trapped by such impurities [79] (and are also slowed by chromium [80]),

the length scale over which the grain boundary effects are significant is unclear; thus, further modelling is required to fully evaluate how much the boundaries are responsible for the low density of loops throughout the grain.

The third possibility that the damage still exists, but as defects too small to resolve clearly in the TEM has been suggested previously as an explanation for defect-free zones in iron and FeCr alloys irradiated with neutrons [11,17,82]. For our analysis, we assigned a conservative minimum size of counted defects to 2 nm in order to reduce ambiguity over loop counting and exclude FIB-damage and oxide. Thus, there may be small dislocation loops (as small as 7 Å [18]) not visible in the micrographs simply due to the foil-quality (see SM-2 and SM-3 for examples of how the contrast from "empty" regions can vary).

In the present study, the visible defects within the helical dislocation were found to contain fewer interstitials than the vacancies absorbed by the helical dislocation core ($7.7 \pm 1.5 \times 10^{25}$ interstitials/m^3 and $3.3 \pm 0.5 \times 10^{26}$ vacancies/m^3, respectively). If interstitial loss from the helix is not significant, then this would mean a large population of interstitial defects remain in this region, existing as clusters too small to be resolved. These could be small dislocation loops, or other configurations such as C15 clusters [73] (which are not visible in weak-beam TEM). If the areas containing visible loops contain a large population of defects not visible to TEM, then it is reasonable to suggest there is a significant invisible population of interstitial (and vacancy) defects in the "empty" regions too.

At higher dose rates, visible loops may nucleate more easily if less damage has recombined, or been lost to sinks. Bhattacharyya et al. [34] studied the same Fe9Cr alloy irradiated at the ATR with the same dose and temperature, but at a slightly higher dose rate of 3.1×10^{-7} dpa/s. The microstructure contained a much more uniform distribution of visible dislocation loops, implying the dose rate effect has a significant effect on the dislocation loop microstructure for only a factor of 3.3.

6. Conclusions

Weak beam dark field TEM examination has been used to investigate the microstructure of a neutron irradiated alloy of Fe9Cr. The microstructure contained irradiation-induced dislocation loops located exclusively around pre-existing dislocations and low angle sub-grain boundaries. Helical dislocations are prominent in the irradiated alloy; these formed from defect-mediated climb of screw dislocations.

We have shown, for the first time, the origin of these helical dislocations in irradiated FeCr is from a vacancy-biased mechanism (at least in the Fe9Cr alloy studied here and for the irradiation parameters used). This supports previous theoretical measurements of the defect bias of screw dislocations that show vacancies should be absorbed more efficiently [31]. The removal of vacancies by the helical dislocations enhances coarsening of interstitial clusters during helical dislocation growth, since less vacancies are available to annihilate with the interstitials. This causes heterogeneity in the spatial distribution of the observable dislocation loops. These findings present a new mechanism for the origin of heterogeneous spatial distributions of interstitial dislocation loops in neutron-irradiated ferritic materials.

Acknowledgements

The authors gratefully acknowledge funding from the UK Engineering and Physical Sciences Research Council under grant numbers EP/L01663X/1, EP/P001645/1, EP/R013136/1 and EP/N007239/1. The authors also acknowledge the UCSB ATR-1 irradiation, and FIB access at the Center for Advanced Energy Studies (CAES) which was supported by the U.S. Department of Energy, Office of Nuclear Energy under DOE Idaho Operations Office Contrast DE-AC07-051D14517 as part of a Nuclear Science User Facilities experiment. Parts of this work were conducted at the Materials Research Facility (UKAEA), supported by equipment funded by National Nuclear Users Facility and the Henry Royce Institute under EP/P021727/1; we are grateful to Dr. Chris Hardie for facilitating this part of the work. We lastly wish to express our thanks to Dr. Mike Jenkins for fruitful discussions on the analysis of the helical dislocations.

Supplementary materials

Supplementary material associated with this article can be found, in the online version, at doi:10.1016/j.actamat.2019.09.031. Data obtained in this study is available from doi:10.5287/bodleian:zBvaedb5X.

References

[1] S.J. Zinkle, J.T. Busby, Structural materials for fission & fusion energy, Mater. Today 12 (2009) 12–19, doi:10.1016/S1369-7021(09)70294-9.
[2] J.L. Boutard, A. Alamo, R. Lindau, M. Rieth, Fissile core and tritium-breeding blanket: structural materials and their requirements, C. R. Phys. 9 (2008) 287–302, doi:10.1016/j.crhy.2007.11.004.
[3] A. Kohyama, A. Hishinuma, D.S. Gelles, R.L. Klueh, W. Dietz, K. Ehrlich, Low-activation ferritic and martensitic steels for fusion application, J. Nucl. Mater. 233–237 (1996) 138–147, doi:10.1016/S0022-3115(96)00327-3.
[4] N. Baluc, R. Schäublin, P. Spätig, M. Victoria, On the potentiality of using ferritic/martensitic steels as structural materials for fusion reactors, Nucl. Fusion 44 (2004) 56–61, doi:10.1088/0029-5515/44/1/006.
[5] D.S. Gelles, Microstructural examination of neutron-irradiated simple ferritic alloys, J. Nucl. Mater. 108–109 (1982) 515 26-515 26, doi:10.1016/0022-3115(82)90523-2.
[6] M. Bachhav, G. Robert Odette, E.A. Marquis, α' precipitation in neutron-irradiated Fe–Cr alloys, Scr. Mater. 74 (2014) 48–51, doi:10.1016/j.scriptamat.2013.10.001.
[7] E.A. Little, D.A. Stow, Void-swelling in irons and ferritic steels, J. Nucl. Mater. 87 (1979) 25–39, doi:10.1016/0022-3115(79)90123-5.
[8] Z. Yao, M.L. Jenkins, M. Hernández-Mayoral, M.A. Kirk, The temperature dependence of heavy-ion damage in iron: a microstructural transition at elevated temperatures, Philos. Mag. 90 (2010) 4623–4634, doi:10.1080/14786430903430981.
[9] C.D. Hardie, C.A. Williams, S. Xu, S.G. Roberts, Effects of irradiation temperature and dose rate on the mechanical properties of self-ion implanted Fe and Fe-Cr alloys, J. Nucl. Mater. 439 (2013) 33–40, doi:10.1016/j.jnucmat.2013.03.052.
[10] C. Pareige, V. Kuksenko, P. Pareige, Behaviour of P, Si, Ni impurities and Cr in self ion irradiated Fe–Cr alloys – comparison to neutron irradiation, J. Nucl. Mater. 456 (2015) 471–476, doi:10.1016/j.jnucmat.2014.10.024.
[11] I.M. Robertson, M.L. Jenkins, C.A. English, Low-dose neutron-irradiation damage in α-iron, J. Nucl. Mater. 108–109 (1982) 209–221, doi:10.1016/0022-3115(82)90489-5.
[12] M. Hernández-Mayoral, C. Heintze, E. Oñorbe, Transmission electron microscopy investigation of the microstructure of Fe–Cr alloys induced by neutron and ion irradiation at 300°C, J. Nucl. Mater. 474 (2016) 88–98, doi:10.1016/j.jnucmat.2016.03.002.
[13] C.A. English, Low-dose neutron irradiation damage in fcc and bcc metals, J. Nucl. Mater. 108–109 (1982) 104–123, doi:10.1016/0022-3115(82)90477-9.
[14] M. Wen, N.M. Ghoniem, B.N. Singh, Dislocation decoration and raft formation in irradiated materials, Philos. Mag. 85 (2005) 2561–2580, doi:10.1080/14786430500154281.
[15] M. Matijasevic, A. Almazouzi, Effect of cr on the mechanical properties and microstructure of Fe–Cr model alloys after n-irradiation, J. Nucl. Mater. 377 (2008) 147–154, doi:10.1016/j.jnucmat.2008.02.061.
[16] W.Y. Chen, Y. Miao, J. Gan, M.A. Okuniewski, S.A. Maloy, J.F. Stubbins, Neutron irradiation effects in Fe and Fe-Cr at 300°C, Acta Mater. 111 (2016) 407–416, doi:10.1016/J.ACTAMAT.2016.03.060.
[17] M. Matijasevic, W. Van Renterghem, A. Almazouzi, Characterization of irradiated single crystals of Fe and Fe–15Cr, Acta Mater 57 (2009) 1577–1585, doi:10.1016/J.ACTAMAT.2008.11.042.
[18] R. Schäublin, B. Décamps, A. Prokhodtseva, J.F. Löffler, On the origin of primary ½ a0 and a0 loops in irradiated Fe(Cr) alloys, Acta Mater. 133 (2017) 427–439, doi:10.1016/J.ACTAMAT.2017.02.041.
[19] H. Trinkaus, B.N. Singh, A.J.E. Foreman, Segregation of cascade induced interstitial loops at dislocations: possible effect on initiation of plastic deformation, J. Nucl. Mater. 251 (1997) 172–187, doi:10.1016/S0022-3115(97)00246-8.
[20] H. Trinkaus, B.N. Singh, A.J.E. Foreman, Mechanisms for decoration of dislocations by small dislocation loops under cascade damage conditions, J. Nucl. Mater. 249 (1997) 91–102, doi:10.1016/S0022-3115(97)00230-4.

[21] R. Schäublin, D. Gelles, M. Victoria, Microstructure of irradiated ferritic/martensitic steels in relation to mechanical properties, J. Nucl. Mater. 307–311 (2002) 197–202, doi:10.1016/S0022-3115(02)01034-6.
[22] E. Hayward, C. Deo, B.P. Uberuaga, C.N. Tomé, C.N.T. Tomeв, The interaction of a screw dislocation with point defects in bcc iron, Philos. Mag. 92 (2012) 2759–2778, doi:10.1080/14786435.2012.674646.
[23] S. Amelinckx, W. Bontinck, W. Dekeyser, F. Seitz, On the formation and properties of helical dislocations, Philos. Mag. 2 (1957) 355–378, doi:10.1080/14786435708243825.
[24] D. Kaoumi, J. Adamson, M. Kirk, Microstructure evolution of two model ferritic/martensitic steels under in situ ion irradiation at low doses (0–2 dpa), J. Nucl. Mater. 445 (2014) 12–19, doi:10.1016/j.jnucmat.2013.10.047.
[25] A. Prokhodtseva, B. Décamps, R. Schäublin, Comparison between bulk and thin foil ion irradiation of ultra-high purity Fe, J. Nucl. Mater. 442 (2013) S786–S789, doi:10.1016/j.jnucmat.2013.04.032.
[26] S.L. Dudarev, J.L. Boutard, R. Lässer, M.J. Caturla, P.M. Derlet, M. Fivel, C.-C. Fu, M.Y. Lavrentiev, L. Malerba, M. Mrovec, D. Nguyen-Manh, K. Nordlund, M. Perlado, R. Schäublin, H. Van Swygenhoven, D. Terentyev, J. Wallenius, D. Weygand, F. Willaime, The EU programme for modelling radiation effects in fusion reactor materials: an overview of recent advances and future goals, J. Nucl. Mater. 386–388 (2009) 1–7, doi:10.1016/j.jnucmat.2008.12.301.
[27] D. Terentyev, D.J. Bacon, Y.N. Osetsky, Reactions between a 1/2⟨111⟩ screw dislocation and ⟨100⟩ interstitial dislocation loops in alpha-iron modelled at atomic scale, Philos. Mag. 90 (2010) 1019–1033, doi:10.1080/14786430903019073.
[28] A. Arsenlis, M. Rhee, G. Hommes, R. Cook, J. Marian, A dislocation dynamics study of the transition from homogeneous to heterogeneous deformation in irradiated body-centered cubic iron, Acta Mater. 60 (2012) 3748–3757, doi:10.1016/J.ACTAMAT.2012.03.041.
[29] D.J. Bacon, Y.N. Osetsky, Modelling dislocation–obstacle interactions in metals exposed to an irradiation environment, Mater. Sci. Eng. A 400–401 (2005) 353–361, doi:10.1016/J.MSEA.2005.01.061.
[30] B.C. Masters, Dislocation loops in irradiated iron, Philos. Mag. 11 (1965) 881–893, doi:10.1080/14786436508223952.
[31] Z. Chang, D. Terentyev, N. Sandberg, K. Samuelsson, P. Olsson, Anomalous bias factors of dislocations in bcc iron, J. Nucl. Mater. 461 (2015) 221–229, doi:10.1016/J.JNUCMAT.2015.03.025.
[32] G.S. Was, Fundamentals of Radiation Materials Science, Springer, 2007, doi:10.1007/978-3-540-49472-0.
[33] K. Nordlund, Historical review of computer simulation of radiation effects in materials, J. Nucl. Mater. 520 (2019) 273–295, doi:10.1016/J.JNUCMAT.2019.04.028.
[34] D. Bhattacharyya, T. Yamamoto, P. Wells, E. Marquis, M. Bachhav, Y. Wu, J. Davis, N. Cunningham, A. Xu, G.R. Odette, Microstructural changes and their effect on hardening in neutron irradiated Fe-Cr alloys, J. Nucl. Mater. 519 (2019) 274–286, doi:10.1016/j.jnucmat.2019.03.022.
[35] J.W. Nielsen, As-run Physics Analysis for the UCSB–1 Experiment in the Advanced Test Reactor, Idaho Falls, ID, United States, 2015. doi:10.2172/1235196.
[36] As-run thermal analysis for the UCSB-1 experiment in the advanced test reactor Project No. 29607, Engineering Calculations and Analysis Report, Idaho National Laboratory, 2015.
[37] J.C. Sublet, J.W. Eastwood, J.G. Morgan, M.R. Gilbert, M. Fleming, W. Arter, FISPACT-II: an advanced simulation system for activation, transmutation and material modelling, Nucl. Data Sheets 139 (2017) 77–137, doi:10.1016/J.NDS.2017.01.002.
[38] L.R. Greenwood, R.K. Smither, SPECTER: Neutron Damage Calculations for Materials Irradiations, Argonne, IL, 1985, doi:10.2172/6022143.
[39] L.A. Giannuzzi, J.L. Drown, S.R. Brown, R.B. Irwin, F.A. Stevie, Applications of the FIB lift-out technique for TEM specimen preparation, Microsc. Res. Tech. 41 (1998) 285–290 doi:10.1002/(SICI)1097-0029(19980515)41:4⟨285::AID-JEMT1⟩3.0.CO;2-Q.
[40] A. Prokhodtseva, B. Décamps, A. Ramar, R. Schäublin, Impact of He and Cr on defect accumulation in ion-irradiated ultrahigh-purity Fe(Cr) alloys, Acta Mater. 61 (2013) 6958–6971, doi:10.1016/j.actamat.2013.08.007.
[41] M. Kirk, X. Yi, M. Jenkins, Characterization of irradiation defect structures and densities by transmission electron microscopy, J. Mater. Res. 30 (2015) 1195–1201, doi:10.1557/jmr.2015.19.
[42] J.C. Haley, TEM of Neutron, Proton and Self-ion Irradiation Damage in FeCr alloys, University of Oxford, 2018 DPhil Thesis.
[43] J. Schindelin, I. Arganda-Carreras, E. Frise, V. Kaynig, M. Longair, T. Pietzsch, S. Preibisch, C. Rueden, S. Saalfeld, B. Schmid, J.-Y. Tinevez, D.J. White, V. Hartenstein, K. Eliceiri, P. Tomancak, A. Cardona, Fiji: an open-source platform for biological-image analysis, Nat. Methods 9 (2012) 676–682, doi:10.1038/nmeth.2019.
[44] W. Cai, V.V. Bulatov, Mobility laws in dislocation dynamics simulations, Mater. Sci. Eng. A 387–389 (2004) 277–281, doi:10.1016/j.msea.2003.12.085.
[45] V.V. Bulatov, W. Cai, Computer Simulations of Dislocations, Oxford University Press, 2006. ISBN 0198526148, 9780198526148.
[46] C.R. Weinberger, G.J. Tucker, Multiscale Materials Modeling for Nanomechanics, Springer, 2016. doi:10.1007/978-3-319-33480-6.
[47] E. Van der Giessen, A. Needleman, Discrete dislocation plasticity: a simple planar model, Model. Simul. Mater. Sci. Eng. 3 (1995) 689–735, doi:10.1088/0965-0393/3/5/008.
[48] H.M. Zbib, M. Rhee, J.P. Hirth, On plastic deformation and the dynamics of 3D dislocations, Int. J. Mech. Sci. 40 (1998) 113–127, doi:10.1016/S0020-7403(97)00043-X.
[49] F. Liu, Z. Liu, P. Lin, Z. Zhuang, Numerical investigations of helical dislocations based on coupled glide-climb model, Int. J. Plast. 92 (2017) 2–18, doi:10.1016/J.IJPLAS.2017.02.015.
[50] B. Bakó, E. Clouet, L.M. Dupuy, M. Blétry, Dislocation dynamics simulations with climb: kinetics of dislocation loop coarsening controlled by bulk diffusion, Philos. Mag. 91 (2011) 3173–3191, doi:10.1080/14786435.2011.573815.
[51] D. Mordehai, E. Clouet, M. Fivel, M. Verdier, Annealing of dislocation loops in dislocation dynamics simulations, IOP Conf. Ser. Mater. Sci. Eng. 3 (2009) 012001, doi:10.1088/1757-899X/3/1/012001.
[52] D.B. Williams, C.B. Carter, Transmission Electron Microscopy: A Textbook for Materials Science, 2nd ed., Springer, 2009. doi:10.1007/978-0-387-76501-3.
[53] P.B. Hirsch, A. Howie, R.B. Nicholson, D.W. Pashley, M.J. Whelan, L. Marton, Electron Microscopy of Thin Crystals, R.E. Krieger Pub. Co, 1977.
[54] M.L. Jenkins, M. Kirk, Characterization of Radiation Damage by Transmission Electron Microscopy (2001) ISBN 0 7503 0748 X (hbk).
[55] D. Hull, D.J.J. Bacon, Introduction to Dislocations, 5th ed., Elsevier BH, 2011. doi:10.1016/B978-0-08-096672-4.00019-0.
[56] L.L. Horton, J. Bentley, K. Farrell, A TEM study of neutron irradiated iron, J. Nucl. Mater. 109 (1982) 222–233, doi:10.1016/0022-3115(82)90490-1.
[57] S.L. Dudarev, A.P. Sutton, Elastic interactions between nano-scale defects in irradiated materials, Acta Mater. 125 (2017) 425–430, doi:10.1016/J.ACTAMAT.2016.11.060.
[58] X. Yi, M.L. Jenkins, M.A. Kirk, Z. Zhou, S.G. Roberts, In-situ TEM studies of 150 keV W+ ion irradiated W and W-alloys: damage production and microstructural evolution, Acta Mater. 112 (2016) 105–120, doi:10.1016/j.actamat.2016.03.051.
[59] A.E. Sand, M.J. Aliaga, M.J. Caturla, K. Nordlund, Surface effects and statistical laws of defects in primary radiation damage: tungsten vs. iron, Europhys. Lett. 115 (2016) 36001, doi:10.1209/0295-5075/115/36001.
[60] J. Weertman, Helical dislocations, Phys. Rev. 107 (1957) 1259–1261, doi:10.1103/PhysRev.107.1259.
[61] R. de Wit, Self-energy of a helical dislocation, Phys. Rev. 116 (1959) 592–597, doi:10.1103/PhysRev.116.592.
[62] G. Wagner, V. Gottschalch, Helical dislocations in sn-doped gap epitaxial layers and their characterization by transmission electron microscopy, Philos. Mag. A Phys. Condens. Matter, Struct. Defects Mech. Prop. 52 (1985) 395–406, doi:10.1080/01418618508237634.
[63] P.M. Anderson, J.P. Hirth, J. Lothe, Theory of Dislocations, 3rd ed., Cambridge University Press, Cambridge, 2017. ISBN 9780521864367.
[64] D. Caillard, J.-L. Martin, Thermally Activated Mechanisms in Crystal Plasticity, 1st ed., Elsevier, Oxford, 2003. ISBN 9780080542782.
[65] F. Ferroni, E. Tarleton, S. Fitzgerald, GPU accelerated dislocation dynamics, J. Comput. Phys. 272 (2014) 619–628, doi:10.1016/J.JCP.2014.04.052.
[66] H. Yu, A. Cocks, E. Tarleton, Discrete dislocation plasticity HELPs understand hydrogen effects in bcc materials, J. Mech. Phys. Solids 123 (2019) 41–60, doi:10.1016/J.JMPS.2018.08.020.
[67] R.W. Balluffi, Mechanisms of dislocation climb, Phys. Status Solidi 31 (1969) 443–463, doi:10.1002/pssb.19690310202.
[68] P. Kroupa, The interaction between prismatic dislocation loops and straight dislocations. Part I, Philos. Mag. 7 (1962) 783–801, doi:10.1080/14786436208212669.
[69] D.H. Thompson, E. Tarleton, S.G. Roberts, S.P. Fitzgerald, Interstitial-mediated dislocation climb and the weakening of particle-reinforced alloys under irradiation, Phys. Rev. Mater. 2 (2018) 080601, doi:10.1103/PhysRevMaterials.2.080601.
[70] M.R. Gilbert, S.L. Dudarev, P.M. Derlet, D.G. Pettifor, Structure and metastability of mesoscopic vacancy and interstitial loop defects in iron and tungsten, J. Phys. Condens. Matter. 20 (2008) 345214, doi:10.1088/0953-8984/20/34/345214.
[71] R.E. Voskoboinikov, MD simulations of collision cascades in the vicinity of a screw dislocation in aluminium, Nucl. Instrum. Methods Phys. Res. Sect. B Beam Interact. Mater. Atoms 303 (2013) 104–107, doi:10.1016/J.NIMB.2013.01.021.
[72] W. Zhou, J. Tian, J. Zheng, J. Xue, S. Peng, Dislocation-enhanced experimental-scale vacancy loop formation in hcp zirconium in one single collision cascade, Sci. Rep. 6 (2016) 21034, doi:10.1038/srep21034.
[73] M.-C. Marinica, F. Willaime, J.-P. Crocombette, Irradiation-Induced formation of nanocrystallites with C15 laves phase structure in bcc iron, Phys. Rev. Lett. 108 (2012) 025501, doi:10.1103/PhysRevLett.108.025501.
[74] S. Xu, Z. Yao, M.L. Jenkins, TEM characterisation of heavy-ion irradiation damage in FeCr alloys, J. Nucl. Mater. 386–388 (2009) 161–164, doi:10.1016/j.jnucmat.2008.12.078.
[75] M.L. Jenkins, Z. Yao, M. Hernández-Mayoral, M.A. Kirk, Dynamic observations of heavy-ion damage in Fe and Fe-Cr alloys, J. Nucl. Mater. 389 (2009) 197–202, doi:10.1016/j.jnucmat.2009.02.003.
[76] S.L. Dudarev, R. Bullough, P.M. Derlet, Effect of the alpha-gamma phase transition on the stability of dislocation loops in bcc iron, Phys. Rev. Lett. 100 (2008) 1–4, doi:10.1103/PhysRevLett.100.135503.
[77] K. Arakawa, M. Hatanaka, E. Kuramoto, K. Ono, H. Mori, Changes in the burgers vector of perfect dislocation loops without contact with the external dislocations, Phys. Rev. Lett. 96 (2006) 1–4, doi:10.1103/PhysRevLett.96.125506.
[78] H. Xu, R.E. Stoller, Y.N. Osetsky, D. Terentyev, Solving the puzzle of 100 interstitial loop formation in bcc iron, Phys. Rev. Lett. 110 (2013) 1–5, doi:10.1103/PhysRevLett.110.265503.
[79] Y. Satoh, H. Matsui, T. Hamaoka, Effects of impurities on one-dimensional mi-

gration of interstitial clusters in iron under electron irradiation, Phys. Rev. B 77 (2008) 094135, doi:10.1103/PhysRevB.77.094135.
[80] K. Arakawa, M. Hatanaka, H. Mori, K. Ono, Effects of chromium on the one-dimensional motion of interstitial-type dislocation loops in iron, J. Nucl. Mater. 329–333 (2004) 1194–1198, doi:10.1016/j.jnucmat.2004.04.263.
[81] D. Terentyev, P. Olsson, L. Malerba, A.V. Barashev, Characterization of dislocation loops and chromium-rich precipitates in ferritic iron–chromium alloys as means of void swelling suppression, J. Nucl. Mater. 362 (2007) 167–173, doi:10.1016/J.JNUCMAT.2007.01.069.
[82] W.-Y. Chen, Irradiation Damage in Neutron-irradiated Fe-Cr Model Alloys, Ph.D. Thesis, University of Illinois Urbana-Champaign, 2014.